JGR Planets

RESEARCH ARTICLE
10.1029/2019JE006271

Key Points:
- Temporal variations of the 365-nm albedo of Venus dominate over any systematic variations along longitude or over local time
- We found no systematic influence by mountains on the 365-nm albedo distribution, in contrast to a previous report

Correspondence to:
Y. J. Lee,
y.j.lee@astro.physik.tu-berlin.de

Citation:
Lee, Y. J., Kopparla, P., Peralta, J., Schröder, S. E., Imamura, T., Kouyama, T., & Watanabe, S. (2020). Spatial and temporal variability of the 365-nm albedo of Venus observed by the camera on board Venus Express. *Journal of Geophysical Research: Planets*, *125*, e2019JE006271. https://doi.org/10.1029/2019JE006271

Received 11 NOV 2019
Accepted 27 APR 2020
Accepted article online 28 MAY 2020

Spatial and Temporal Variability of the 365-nm Albedo of Venus Observed by the Camera on Board Venus Express

Y. J. Lee[1], P. Kopparla[2], J. Peralta[3], S. E. Schröder[4], T. Imamura[2], T. Kouyama[5], and S. Watanabe[6]

[1]Zentrum für Astronomie und Astrophysik, Technische Universität Berlin, Berlin, Germany, [2]GSFS, The University of Tokyo Kashiwa Campus, Kashiwa, Japan, [3]ISAS/JAXA, Sagamihara, Japan, [4]DLR, Berlin, Germany, [5]AIST, Tokyo, Japan, [6]Space Information Center, Hokkaido Information University, Ebetsu, Japan

Abstract We mapped the distribution of the 365-nm albedo of the Venus atmosphere over the years 2006–2014, using images acquired by the Venus Monitoring Camera (VMC) on board Venus Express. We selected all images with a global view of Venus to investigate how the albedo depends on longitude. Bertaux et al. (2016, https://doi.org/10.1002/2015JE004958) reported a peak in albedo around 100° longitude and speculated on an association with the Aphrodite Terra mountains. We show that this peak is most likely an artifact, resulting from long-term albedo variations coupled with considerable temporal gaps in data sampling over longitude. We also used a subset of images to investigate how the albedo depends on local time, selecting only south pole viewing images of the dayside (local times 7–17 hr). Akatsuki observed mountain-induced waves in the late afternoon at 283 nm and 10 μm (Fukuhara et al., 2017, https://doi.org/10.1038/ngeo2873). We expect that the presence of such waves may introduce 365-nm albedo variations with a periodicity of one solar day (116.75 Earth days). We searched for such a periodicity peak at 15:30–16:00 local time and low latitudes but did not find it. In conclusion, we find that temporal albedo variations, both short and long term, dominate any systematic variations with longitude and local time. The nature of VMC dayside observations limits regular data sampling along longitudes, so longitudinal variations, if they exist, are difficult to extract. We conclude that any influence by the Venus surface on 365-nm albedo is negligible within this data set.

Plain Language Summary Recently, it was reported that mountains on the surface of Venus can affect the atmosphere at the altitude of the cloud tops (70 km). For example, the brightness of the clouds (albedo) in images made by the Venus Express spacecraft at ultraviolet wavelengths (365 nm) was suspected to peak over a high mountain, Aphrodite Terra. We searched for such surface effects using the Venus Express images taken at 365 nm over the years 2006–2014. We found that the albedo was strongly variable over this period and that different longitudes were systematically imaged at different times. It is therefore not possible to uncover the influence of mountains on the albedo, and we believe that the reported albedo peak near Aphrodite Terra is most likely not real. Another spacecraft, Akatsuki, observed global-scale atmospheric waves in the late afternoon that are originated by mountains. We also searched for albedo changes at the same latitude with a period of one solar day (116.75 Earth days) that might be linked with these atmospheric waves but did not find any period above the noise level. We conclude that the influence of mountains on the 365-nm albedo is too weak to be recognized in Venus Express images.

1. Introduction

Venus images at 365 nm reveal distinct dark and bright patches that were observed for the first time in the 1920s (Ross, 1928; Wright, 1927). The dark patches are caused by an unidentified absorber (hereafter, "unknown absorber") located near the cloud top level at 60- to 70-km altitude (Esposito, 1980; Tomasko et al., 1980; Ragent et al., 1985). Suggested candidates for the absorber are $FeCl_3$, S_x, OSSO, and S_2O (Mills et al., 2007; Frandsen et al., 2016; Krasnopolsky, 2017), and even biological pigments (Limaye et al., 2018). An absorption feature in the Venus reflectance spectrum that covers wavelengths from the ultraviolet to the visible is associated with the unknown absorber (Tomasko et al., 1980; Pérez-Hoyos et al., 2018; Marcq et al., 2020). The smooth nature of the absorption feature, that is, the absence of narrow absorption lines, has made it difficult to clarify the absorber's chemical composition (Krasnopolsky, 2017; Pérez-Hoyos et al., 2018).

Its broad nature makes the unknown absorber an important agent in solar energy absorption calculations (Crisp, 1986; Lee et al., 2019).

The spatial distribution of the unknown absorber is patchy and has been used to retrieve cloud-tracked wind vectors (Rossow et al., 1980; Khatuntsev et al., 2013; Kouyama et al., 2013; Hueso et al., 2015; Horinouchi et al., 2018). Bertaux et al. (2016) analyzed winds retrieved from VMC images published by Khatuntsev et al. (2013) and found an influence of surface topography on the wind vectors at 365 nm at the cloud top level. The authors showed that over Aphrodite Terra (40–160° longitude, 5–15°S latitude), the winds are slower and the albedo is higher. They explained this as gravity waves propagating from the mountains and breaking up in the cloud layer. This wave breaking decelerates the horizontal wind, and this causes the convergence of winds that suppresses the vertical transport of the unknown absorber. This would result in a lower abundance of the absorber, meaning higher albedo (Bertaux et al., 2016). The same explanation would apply to the H_2O gas distribution (Fedorova et al., 2016). There are other reports suggesting possible surface influences near the cloud top level. Wave packets observed at 365 nm on the dayside were concentrated over high-elevation areas in the northern hemisphere (Piccialli et al., 2014). Near-infrared nightside observations showed stationary features over areas with high elevations (Peralta et al., 2017). Images of Akatsuki at 10 μm showed a planetary-scale stationary wave over Aphrodite Terra (Fukuhara et al., 2017; Kouyama et al., 2017). Results that are inconsistent with Bertaux et al. (2016) have also been reported. For example, cloud top level winds derived from Akatsuki data at 283 and 365 nm showed no correlation with surface elevation (Horinouchi et al., 2018; Imai et al., 2019). While the topography-induced planetary-scale stationary waves are visible at 283 nm and 10 μm, they were seen only once at 365 nm (Kitahara et al., 2019). This implies that the topography has a negligible impact on the horizontal distribution of the unknown absorber. In addition, the planetary-scale stationary waves clearly depend on local time; their amplitude increases over the afternoon and decreases after sunset (Kouyama et al., 2017). These properties can be explained by diurnal variations in gravity wave formation by air passing over the mountain ridge (Navarro et al., 2018).

Recently, long-term variations of 365-nm albedo were reported, changing by a factor of 2 over the last decade (Lee et al., 2019). These long-term albedo variations would affect the mean albedo map shown by Bertaux et al. (2016), because the longitudinal coverage of dayside images progressed slowly following the slow rotation of the planet. Therefore, we investigate spatial and temporal variations of the 365-nm albedo in images of the Venus Monitoring Camera (VMC) of Venus Express over the years 2006–2014 and investigate the impact of surface topography. In this way, we may characterize the mountain-induced waves, for example, what atmospheric parameters are correlated with the surface and how are they associated with the vertically propagating waves? Moreover, if we can extract the solar phase angle dependence of scattering by cloud aerosols along longitude and latitude, then we can make a map of aerosol properties, such as microphysical properties.

2. Data and Methods

2.1. Data Selection

VMC operated from April 2006 to 2014 (Markiewicz et al., 2007). Venus Express had an elliptic polar orbit with an apocenter over the southern polar region at a distance of ~66,000 km from the planet and a pericenter over the northern polar region with altitudes ranging 200 from 300 km. This orbit allowed a global monitoring of the southern hemisphere. The orbital period of Venus Express was 24 hr, and the global monitoring was done over several hours per day. We selected these global view images, taken at off-pericenter, when the distance of the spacecraft from the planet was larger than 34,000 km (Lee et al., 2015). VMC had four channels at 365, 513, 965, and 1,000 nm with a 40-nm band width (Markiewicz et al., 2007). We used the 365-nm UV channel, targeting the unknown absorber. We used Planetary Science Archive (PSA) Level 2 data in this study, which are calibrated images given in units of radiance.

We selected data that satisfy the following conditions. First, we restricted images with exposure times shorter or equal to 0.016 s, to avoid saturation. Second, we used images without recognizable artifacts that were reported in Titov et al. (2012). Third, we considered images having a full visible area of illumination, without being cut in parts by the boundaries of the field of view (FOV). The last condition in particular ensures that all local times are present within one image, which will be discussed in section 3.2. These three conditions are the same as those used in previous studies (Lee et al., 2015, 2019); 17,742 images satisfy the conditions

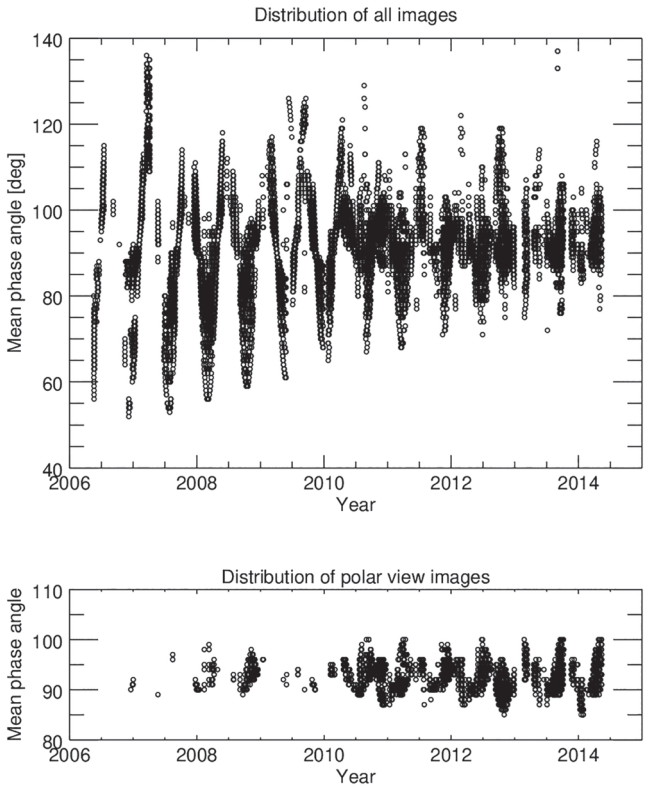

Figure 1. Distributions of selected images over time and phase angle. (upper) All images. (lower) All polar view images.

above. The data span 8 years, from May 2006 to May 2014, and the angle of the Sun, Venus, and VMC (phase angle) ranges from 52° to 137° (Figure 1).

We prepared a subset of the data, applying an additional condition to have a polar view, defined as

$$\text{polar view} \begin{cases} e_{\max}(\theta < 50°\text{S}) < 50° \\ e_{\min}(30°\text{S} < \theta < 30°\text{N}) > 60° \end{cases}, \quad (1)$$

where $e_{\max}$ and $e_{\min}$ are the maximum and minimum of emergence angles, respectively, and θ is the latitude. This condition sorts out polar viewing geometries. An example of a polar view image is shown in Figure 2 (lower panels), which covers all local times of the dayside in one image. A total of 3,466 images satisfies the polar view condition in the 85–105° phase angle range (Figure 1).

2.2. Calibration and Photometric Correction

This study uses the equigonal albedo A (Shkuratov et al., 2011) (hereafter, albedo) that is derived from measured radiance using the following procedure. We first convert the measured radiance R_{obs} (W m^{-2} sr^{-1} μm^{-1}) into a radiance factor r_{F} as

$$r_{\text{F}} = \pi\beta R_{\text{obs}} \frac{{d_{\text{V}}}^2}{S_{\odot}}, \quad (2)$$

where β is a calibration correction factor for VMC, d_{V} is the distance of Venus to the Sun in AU, and $S_{\odot}$ is the average solar flux (W m^{-2} μm^{-1}) in the UV filter of VMC at 1 AU. The solar irradiance is taken from the Smithsonian Astrophysical Observatory reference spectrum 2010 (SAO2010) (Chance & Kurucz, 2010). An updated calibration correction factor is applied in this study: $\beta = 1.58$ (Lee et al., 2019), which was derived from the cross-comparisons of VMC with MESSENGER and Hubble Space Telescope observations in 2007 and 2011, respectively, and then validated using the disk-integrated albedo derived from VMC and Akatsuki observations in 2011. A calibration correction factor of 2.34 was derived from a comparison between VMC and VIRTIS (Shalygina et al., 2015; Titov et al., 2012) and was applied to the data published at the PSA. We do not use 2.34, because VIRTIS had not yet been fully calibrated when this corrective constant was derived (Carlson et al., 2016). Shalygina et al. (2015) also introduced an additional, time-dependent correction factor, interpreting the Venus brightness change as a filter degradation. While we do not use this additional correction factor in this paper, we investigate the sensitivity of our results to this factor in Appendix A and show that it does not affect our main conclusions.

The radiance factor r_{F} is a function of incidence i, emergence e, and phase α angles. We define $\mu_0 = \cos(i)$ and $\mu = \cos(e)$ and separate the radiance factor $r_{\text{F}}(\mu, \mu_0, \alpha)$ into a disk function $D(\mu, \mu_0, \alpha)$ and an albedo $A(\alpha)$ (Shkuratov et al., 2011) as

$$r_{\text{F}}(\mu_0, \mu, \alpha) = A(\alpha)D(\mu, \mu_0, \alpha), \quad (3)$$

where the disk function D describes the brightness distribution over the Venus disk. We limit our analysis to pixels having $e < 81°$ and $i < 84°$ (Lee et al., 2015). We use the combined Lambert and Lommel-Seeliger law (LLS) (Buratti & Veverka, 1983; McEwen, 1986) for the disk function D because of its slightly better performance compared to the Lambert or Minnaert laws (Lee et al., 2015; 2017). D is defined as

$$D = k_{\text{LLS}}(\alpha)\frac{2\mu_0}{\mu_0 + \mu} + [1 - k_{\text{LLS}}(\alpha)]\mu_0, \quad (4)$$

where k_{LLS} is the factor between 0 and 1. k_{LLS} depends on phase angle α in degree as

$$k_{\text{LLS}}(\alpha) = 0.216004 + 0.00194196 \times \alpha - (2.11589 \times 10^{-5}) \times \alpha^2 \quad (5)$$

as previously derived from a fit to a large number of UV images (Lee et al., 2019). In this way, we calculated the albedo A for all images.

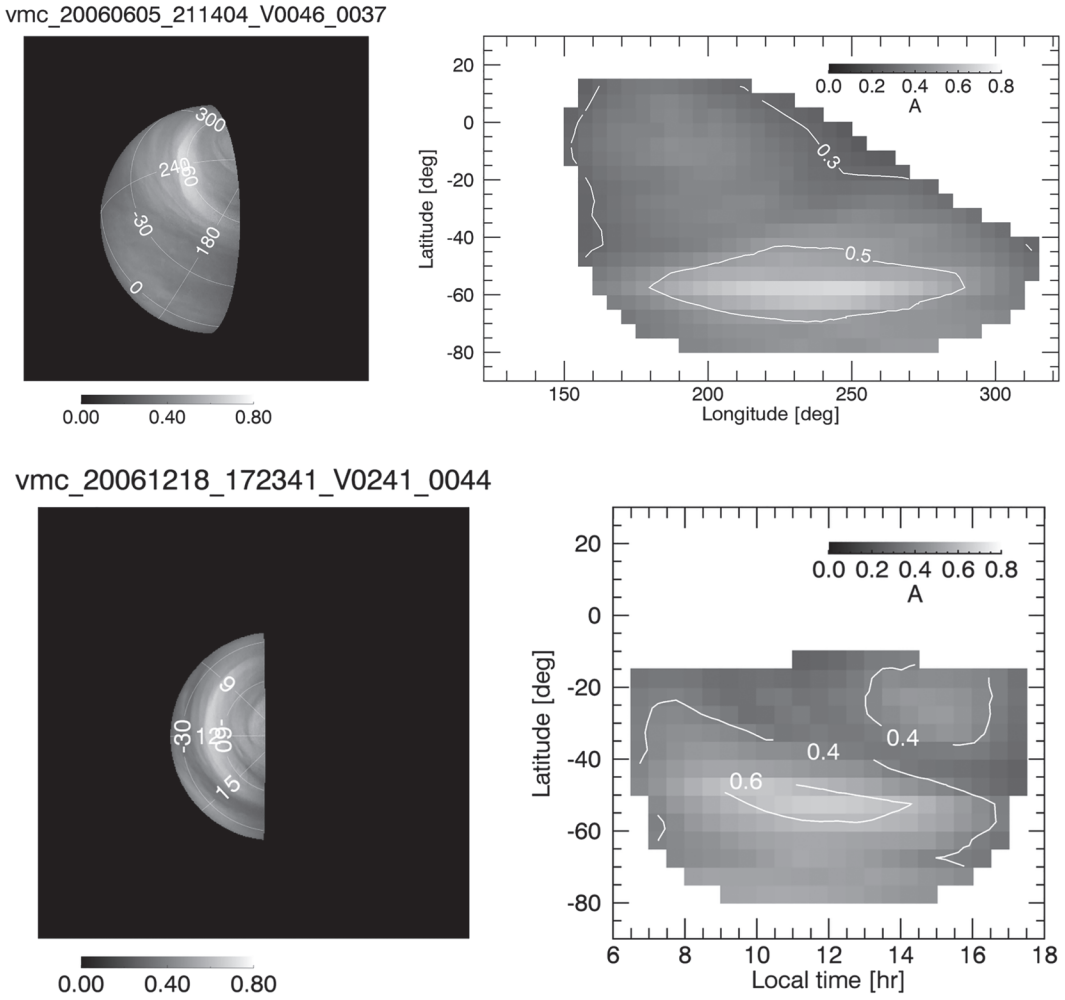

Figure 2. Example of albedo images used in the analysis. (top left) Albedo reconstructed from a VMC image taken at 21:14:04 UTC 5 June 2006 (Orbit 46 and Image 37). (top right) Albedo map of the top left image binned along longitude and latitude. (bottom left) Polar view albedo reconstructed from a VMC image taken at 17:23:41 UTC 18 December 2006 (Orbit 241 and Image 44). (bottom right) Polar view albedo map of the bottom left image binned along local time and latitude. Local time is in hours.

2.3. Grids of Phase Angle, Latitude, Longitude, and Local Time

The albedo A depends on solar phase angle α, due to strong forward or backward scattering by cloud aerosols (Mie scattering). Therefore, we group the data into 5°-wide phase angle bins, and all comparisons are done with these bins. We apply two different binning schemes, one for the entire data set and the second for the subset of south pole viewing images (section 2). For the first scheme, we rebin all albedo images into a 5° longitude × 5° latitude grid and analyze the albedo distribution in section 3.1. The top panels of Figure 2 show the original albedo image (left) and the rebinned albedo map (right). So the data are distributed as a function of phase angle, observation time, latitude, and longitude. For second binning scheme, we rebin all albedo images into a 30-min local time × 5° latitude grid and analyze the albedo distribution in section 3.2. These subset of data are a function of phase angle, observation time, latitude, and local time. The bottom panels of Figure 2 show the original albedo image (left) and the rebinned albedo map (right). So these data are distributed as a function of phase angle, observation time, latitude, and local time. We use only bins with ≥30 valid pixels to improve the signal-to-noise.

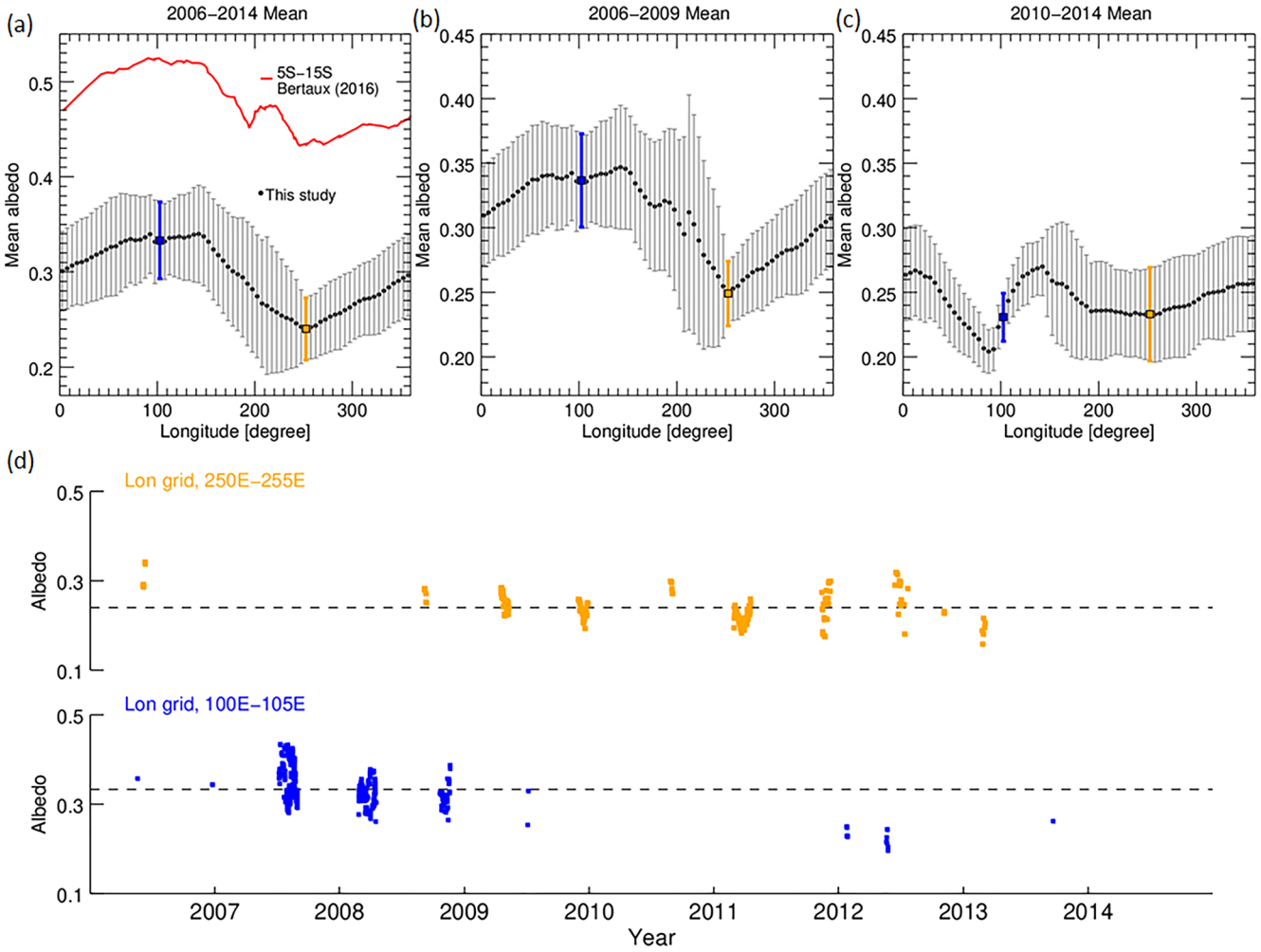

Figure 3. Mean albedo as a function of longitude at 10–15°S latitude and 75–80° phase angle. (a) Mean albedo in 2006–2014. (b) Mean albedo in 2006–2009. (c) Mean albedo in 2010–2014. (d) Time series of albedo at 100–105°E (blue symbols) and 250–255°E (orange symbols). The red curve in (a) is the mean albedo at 5–15°S from Bertaux et al. (2016) (their Figure 10). The dashed horizontal lines in (d) indicate the mean values in 2006–2014.

3. Results

3.1. Longitudinal Dependence of Mean Albedo

We find that the mean albedo over the years 2006–2014 along longitude at 75–80° phase angle is high over Aphrodite Terra (40–160° longitude, Figure 3a). This is consistent with the result reported by Bertaux et al. (2016). The red curve is taken from their Figure 10, using center values of their data range. Their mean albedo is much higher than ours. There are several possible reasons: Their calibration correction factor and phase angle and image selection criteria are likely different from ours but are not reported in their paper. Also, the authors used a different photometric correction (Lambertian).

A recent study reported global-scale, long-term variations of the 365-nm albedo (Lee et al., 2019). Such variation can affect the longitudinal dependence of the albedo, determined by how the data are distributed over time. Therefore, we check how the data are distributed over the years in Figure 3d. We show time series for two longitude ranges: 100–105° and 250–255°, in which we found the maximum and minimum mean albedo values, respectively. The full time series (Figure 3d) shows that the temporal sampling was different for the two ranges. Many data points in the 100–105° range were collected before 2008, when Venus was relatively bright. But those in the 250–255° range were collected between 2009 and 2012, when Venus was relatively dark. So, the longitudinal albedo trend can be completely different depending on the selected time range. The longitudinal trend over the entire Venus Express mission (2006–2014, Figure 3a) and that over the first half (2006–2009, Figure 3b) are similar. The time series shows that there are no data points in 2007

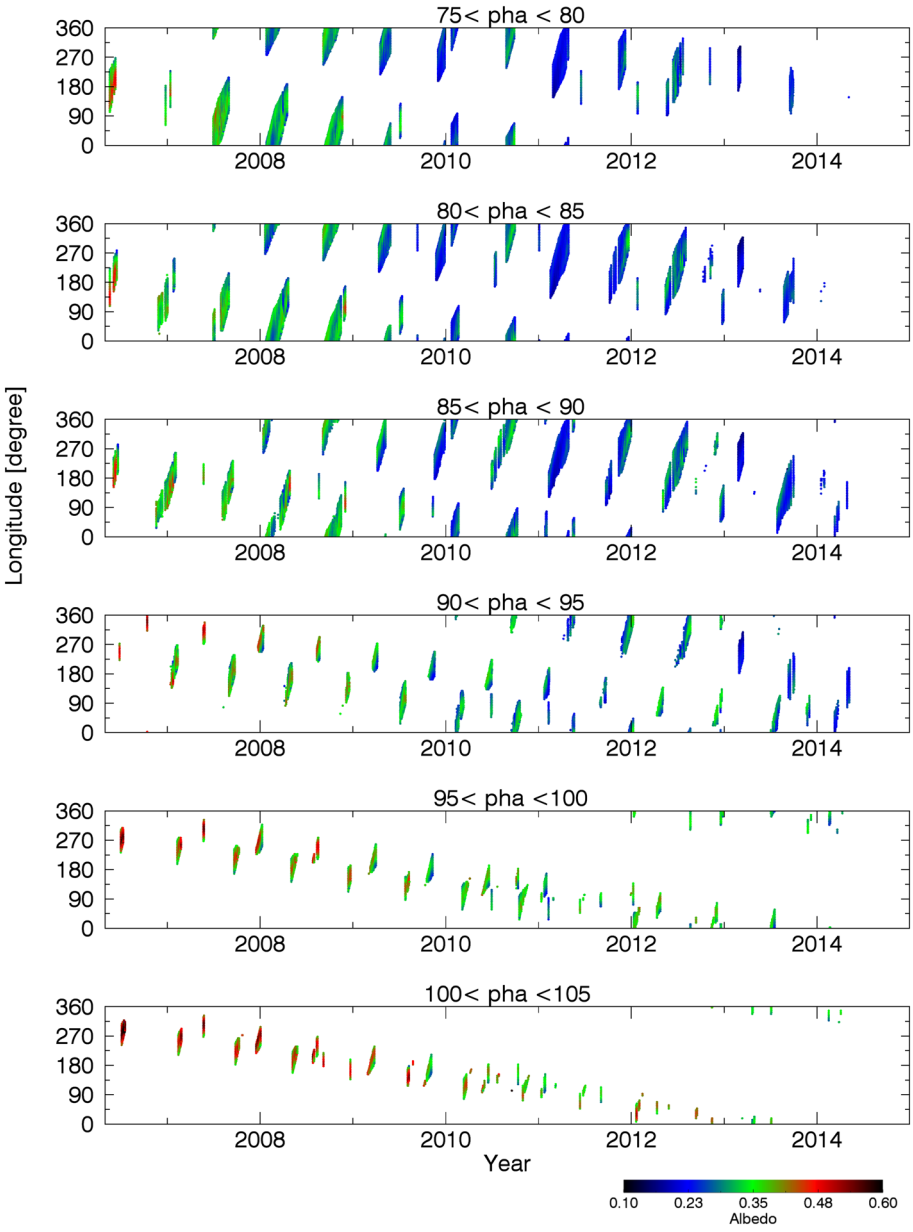

Figure 4. Albedo distributions at 10–15°S latitude as a function of longitude (0–360°) and observation time (2006–2014) for six phase angle bins.

in the 250–255° longitude range, but there are points in the 100–105° range. The trend over the second half of the mission is completely different (2010–2014, Figure 3c). The time series shows that the data points in the 100–105° range were acquired mostly in 2012, although their number is small. The data were sampled closely in time for the two longitude ranges, and the mean albedo is similar for both. We conclude that the high albedo in 2007 is responsible for the high mean albedo over the entire mission in the 100–105° range.

We find that the mean albedo in the 10–15°S latitude range was higher before 2008 than after 2010. Now, we will look at how the albedo is distributed along longitude for other phase angle bins. For the six bins in the 75° to 105° range, Figure 4 shows the distributions of albedo. We find a similar albedo trend for each bin. The figure also shows that the longitudinal data coverage changed slowly over the years. Figure 5 shows the mean albedo at 10–15°S latitude for each phase angle bin, calculated for the three observational periods we introduced in Figure 3. For the higher phase angle bins (>90°), the mean albedo trend is opposite from the longitudinal trend in Bertaux et al. (2016) for the entire 2006–2014 period and for the first half (2006–2009).

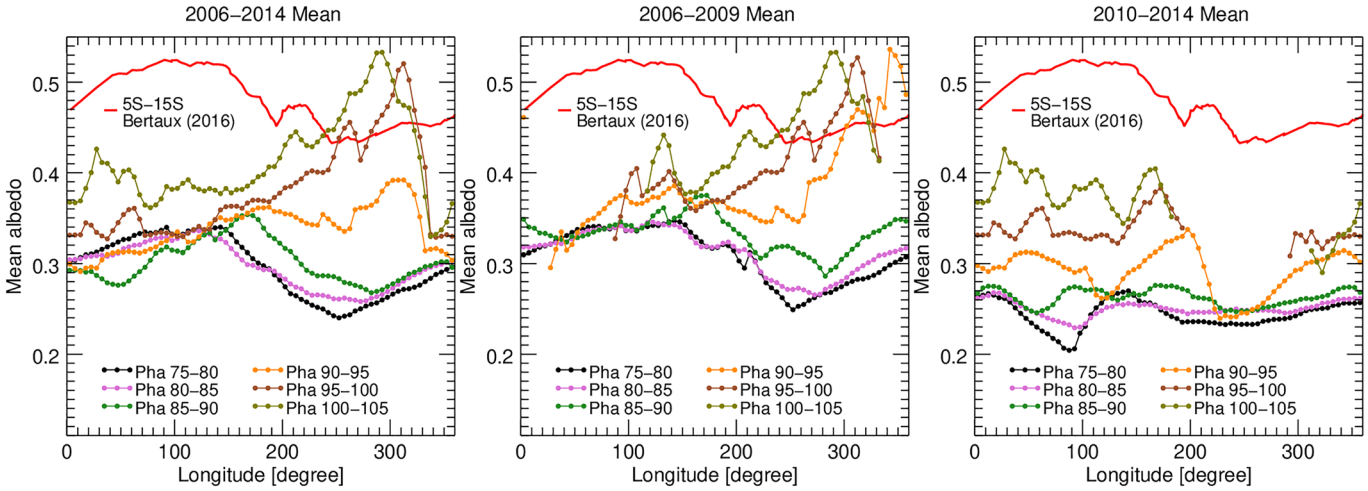

Figure 5. Mean albedo as a function of longitude at 10–15°S latitude for the phase angle bins between 75° and 105°. (left) 2006–2014. (center) 2006–2009. (right) 2010–2014. The red curve is the mean albedo at 5–15°S from Bertaux et al. (2016) (their Figure 10).

Therefore, the selection of time period and phase angle for the data affects the trend of the mean albedo along longitude.

Figure 6 shows maps of the mean albedo over the entire 2006–2014 period for six phase angle bins. The number of images used to make the maps is 967, 1,429, 3,173, 5,815, 3,127, and 1,121 for the phase angle bins from 75° to 105°. All maps have a similar appearance: dark at low latitudes and bright at high latitudes. However, there are subtle differences between the phase angle ranges. These are caused by the irregular distribution of data over longitude and time (Figure 4). The sensing altitudes increase as the phase angle increases due to the stronger scattering efficiency of aerosols. If there was a surface influence on physical conditions of the atmosphere at the cloud top level, then we could learn about the number density and microphysical properties of aerosols. However, the irregular data distribution obscures such phase angle dependence in these mean albedo maps. The high albedo areas have a slightly larger standard deviation, as shown on the right side of Figure 6. This is related to the large temporal variations associated with the "cold-collar" feature (Titov et al., 2012).

3.2. Local Time Dependence of Mean Albedo

We compare the mean albedo versus local time at different latitudes using a subset of the data: images with a polar view as defined by equation (1) (Figure 2 bottom panels). The polar view images cover all local times simultaneously; therefore, long-term variations will not obscure a possible dependence of the albedo on local time.

Figure 7 shows the mean albedo as a function of local time in three latitude ranges: 30–35°S, 50–55°S, and 70–75°S. The three latitudinal bins in the left column show the typical latitudinal albedo variations: dark at low latitudes and bright at high latitudes. The standard deviations (error bars in the figure) of the data points are large due to strong temporal variations for all local times and latitudes. The three time series in the right column show these variations for three local time ranges: 8:00–8:30 (morning), 11:30–12:00 (noon), and 15:30–16:00 (afternoon). Interestingly, each local time bin shows the similar short-term variations. The superrotating atmosphere near the cloud top level may create these similar variations.

In the mean albedo plot in Figure 7 for 30–35°S latitude, there is a subtle local minimum around noon. The albedo plots at other latitudes have a peak near local noon. However, this local time dependence may be an artifact of viewing geometry, as we used only south pole viewing images. We repeat our analysis with images of the UV imager (UVI) on board Akatsuki (Yamazaki et al., 2018), which observes Venus from the equatorial plane. We use the same data grid and the same photometric correction. The UVI equator viewing images cover only half of the dayside at once, either morning or afternoon, so we do the comparison for both sides. We select data for 1 year for each instrument, 2008 for VMC and 2016 for UVI, because the global UV albedo levels in these 2 years were reasonably similar (Lee et al., 2019). We applied the same selection

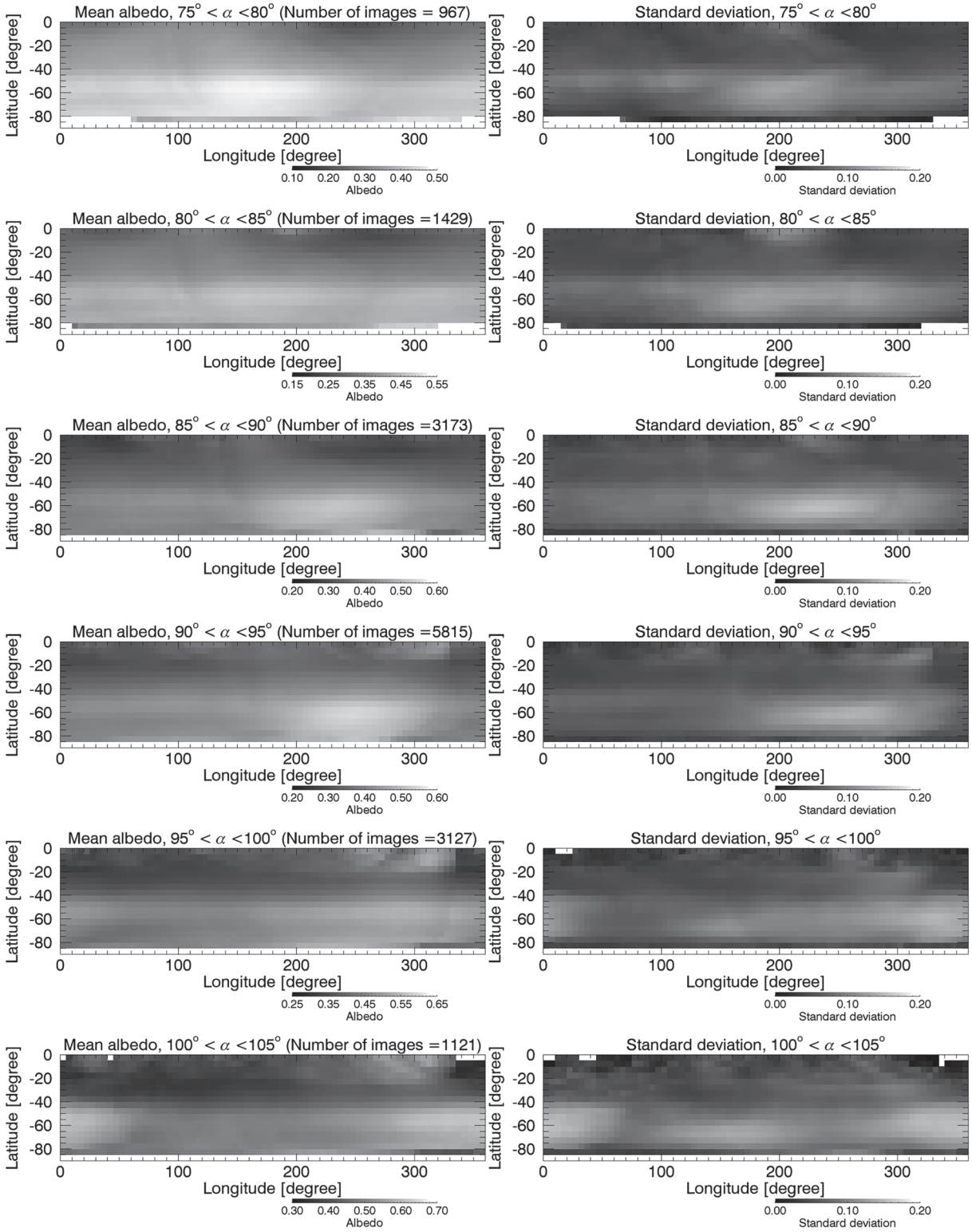

Figure 6. Mean albedo maps (left column) and standard deviations (right column) for six phase angle bins, indicated in the top of each panel. The number of images used is shown in the top of each panel on the left column.

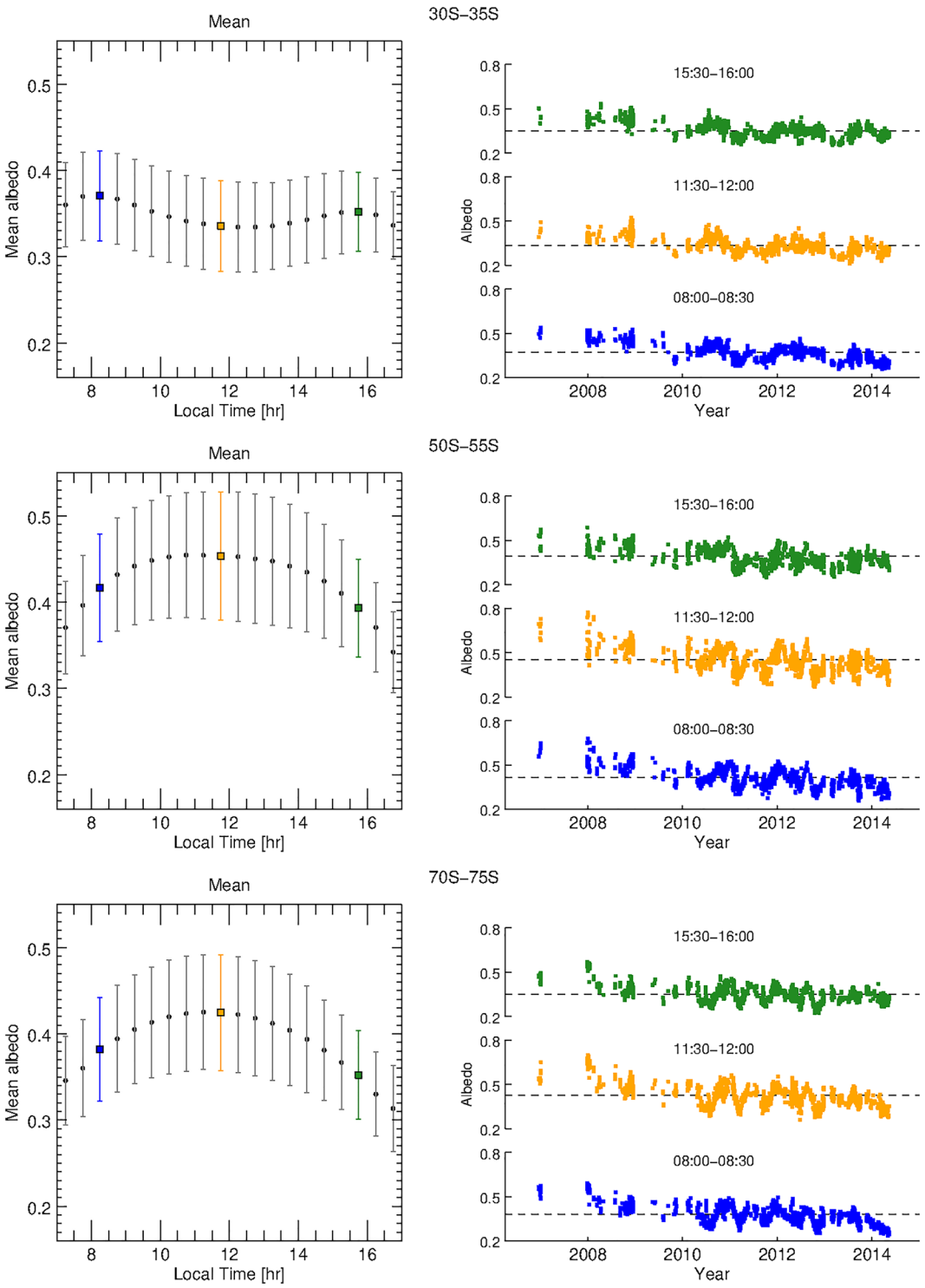

Figure 7. Mean albedo as a function of local time from 7 to 17 hr (left column) and time series at three selected local times (right column). (top) 30–35°S. (middle) 50–55°S. (bottom) 70–75°S. The blue, orange, and green symbols represent data for the 8:00–8:30, 11:30–12:00, and 15:30–16:00 local time periods, respectively. The horizontal dashed lines in the right panels indicate the mean albedo. The error bars are the standard deviations. The phase angle of all data is 90–95°.

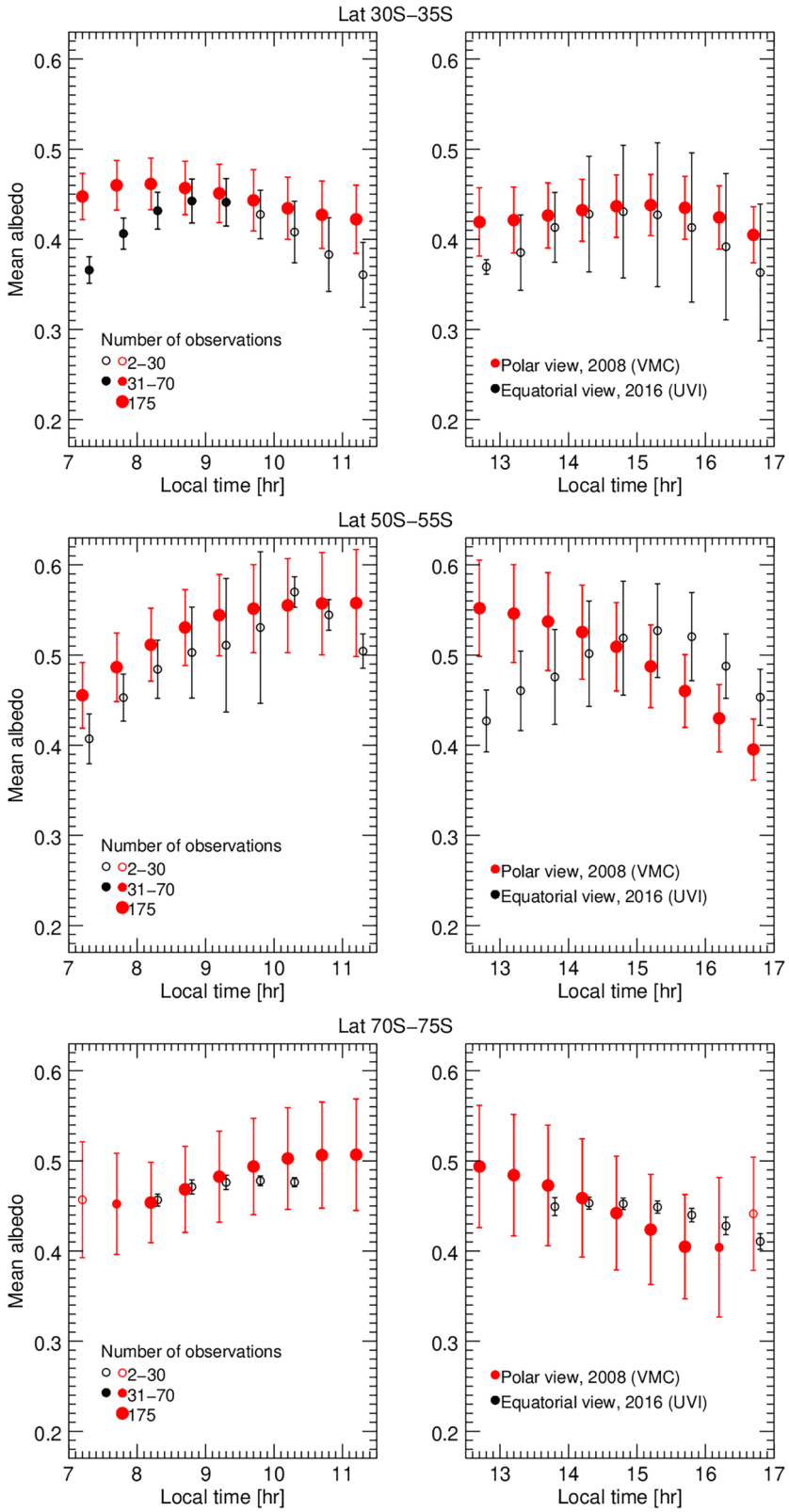

Figure 8. The mean albedo in the polar view geometry of VMC in 2008 (red circle) and the equatorial view of UVI in 2016 (black circle) at 90–95° phase angle. UVI can observe either the morning or afternoon side. The morning and afternoon sides are in the left and right columns, respectively. The symbol size indicates the number of observations per bins used to calculate the mean albedo. (top) Latitude 30–35°S. (middle) Latitude 50–55°S. (bottom) Latitude 70–75°S.

criteria to both UVI and VMC images. The comparison is shown in Figure 8. The maximum number of data points is 175 for VMC and 31 for UVI for the local time bins in Figure 8. We find similar levels of albedo for the two image sets in all three latitude ranges. Differences between the two sets appear near noon at 30–35°S and 50–55°S (UVI noon time data are not available at 70–75°S). These may be related with imperfect photometric correction at large incidence angles in the UVI images at 90° phase angle or can be due to temporal variations in case of small numbers of UVI images. The subtle local minimum at 30–35°S might be real, as they are shared by both image sets. However, we cannot quantify this local time dependency.

4. Discussion

4.1. Longitudinal Albedo Trend

We have analyzed the 365-nm albedo as a function of longitude and observation time (Figure 4) and found both strong long-term variations for all phase angle bins and irregular longitude coverage over time. Because of these variations, maps of the mean albedo over 2006–2014 (Figure 6) are different for each phase angle bin. The mean albedo along longitude changes depending on the selected time range for the images analyzed (Figure 3). This suggests that the longitudinal dependence reported by Bertaux et al. (2016) is an artifact. To extract a possible longitudinal dependence, one needs good temporal coverage data over all longitudes to avoid mixing with temporal variations. But such data are impossible to acquire, due to the nature of dayside observations on Venus.

Our results are consistent with several recent results. Encrenaz et al. (2019) reported no clear longitudinal trend in the distribution of SO_2 gas above the clouds from ground-based observations. Horinouchi et al. (2018) found no such trend for the UV wind fields from December 2015 to March 2016 and neither did Imai et al. (2019) for the winds in 2017. A reanalysis of data of the UV spectrometer (SPICAV) on board Venus Express found that for the distribution of SO_2 gas, it is difficult to distinguish between longitudinal and temporal variations (Marcq et al., 2020). On the other hand, our results are inconsistent with the correlation of the H_2O distribution with surface topography at low latitudes (Fedorova et al., 2016).

Obvious mountain-induced waves at the cloud top level were seen in images acquired by Akatsuki's Long-wave Infrared Camera (LIR) (Fukuhara et al., 2017) and UVI at 283 nm (Kitahara et al., 2019). Images at 365 nm do not show such waves. Kitahara et al. (2019) explained their absence by proposing that the cloud aerosols and the unknown absorber (365 nm) have similar scale heights, whereas that of the SO_2 gas (283 nm) is smaller. We note that stationary mountain-induced waves were observed near the cloud top level by LIR and 283-nm images. The waves should have large intrinsic phase speeds at the level because of the fast background superrotation. The waves are propagating upwards at the cloud level with fast vertical group velocities and with a relatively long vertical wavelength, compared to the depth of cloud convective layer. Therefore, the mountain-induced waves may not affect the zonal wind speed at this altitude a lot (Horinouchi et al., 2018; Imai et al., 2019) and thereby the vertical transport of the unknown absorber.

4.2. Local Time Trend of Albedo

Previous observations suggest that some conditions at the cloud top level depend on local time. The wind speed as derived from both Venus Express and Akatsuki observations was found to depend on local time (Hueso et al., 2015; Horinouchi et al., 2018). Small-size aerosols with an effective radius of 0.23 μm, as derived from near-infrared VMC images, were found only in the morning (Shalygina et al., 2015). The scale height and radius of the upper haze do not show significant local time variations between morning and evening (Luginin et al., 2016). Our results show that the local time dependence of the 365-nm albedo is not significant, as temporal variations dominate. We noticed only a subtle local minimum at low latitudes.

Recent studies on the distribution of SO_2 gas above the clouds report that the SO_2 abundance at low latitudes is lower around noontime (Encrenaz et al., 2019; Marcq et al., 2020). It is tempting to connect these observations with our local time trend at 30–35°S in Figure 7, with its subtle local minimum around noon. This may be related with the anticorrelation between the abundances of SO_2 gas and the unknown absorber near the cloud top level (or the correlation between SO_2 gas abundance and the UV reflectivity) (Lee et al., 2019; Marcq et al., 2020). However, we cannot quantify the absolute level of local time dependence with the current photometric correction (section 3.2).

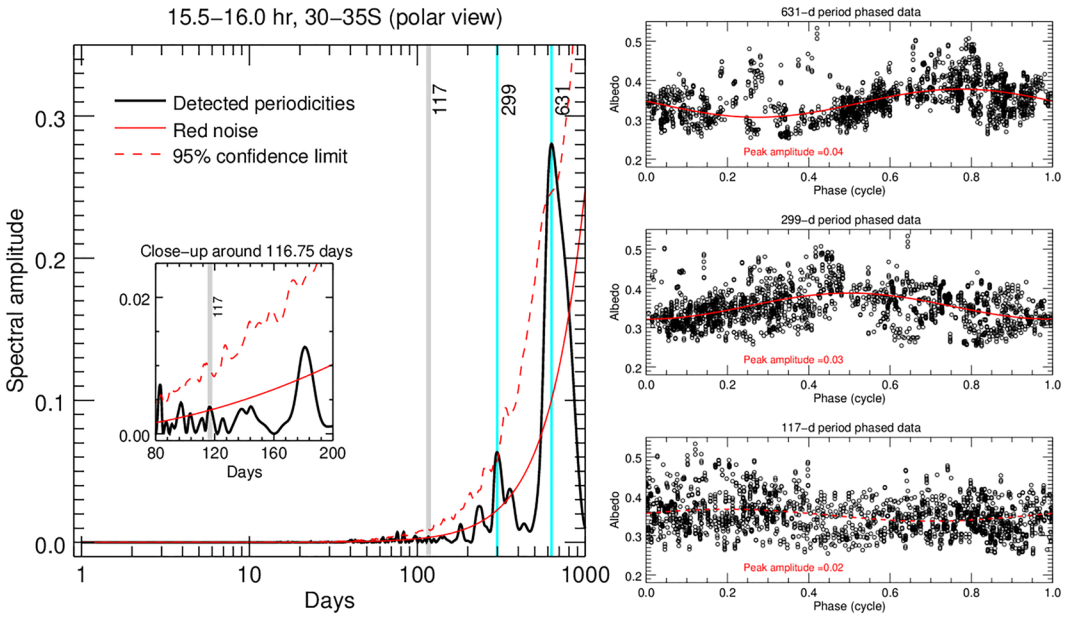

Figure 9. Lomb-Scargle periodograms at 30–35°S latitude for polar view images in the afternoon (15:30–16:00, left). The time series of these data are shown in Figure 7. Cyan lines indicate the detected peaks at ~300 and 630 days over the 95% confidence limit (red dashed line). The red solid lines indicate the red noise level (see text for details). Amplitude has an arbitrary unit. The right column shows the original albedo data as a function of phase at the detected periods: 631 day (upper right) and 299 days (middle right). Their sinusoidal model fit is shown together in red curves. The 117-day peak is missing, as shown in the enlarged plot (left) and its phased data (bottom right).

4.3. Periodicity of Albedo as a Function of Local Time

We calculate the Lomb-Scargle periodograms, as described in Kopparla et al. (2019), taking into account red noise. Atmospheric data are characterized by red noise, which occurs in time series that are autocorrelated. The power in the red noise spectrum increases with decreasing frequency (Gilman et al., 1963). Thus, white noise spectra, which are flat with respect to frequency, are not appropriate to determine significance against noise for atmospheric time series. To determine the appropriate level of red noise for the given data, the correlation between data one time step apart must be known first. For regular time series, the degree of autocorrelation is easily estimated by fitting routines, but problems arise when the time series is spaced irregularly. Interpolation to convert the irregular series to a regular one is not appropriate since this further "reddens" the time series by introducing low-frequency noise.

Schulz and Mudelsee (2002) devised a method to estimate the degree of autocorrelation directly from data for an irregularly spaced time series. Using this estimated degree of autocorrelation, several pure red noise time series with no periodicity are generated in a Monte Carlo-type procedure (in this study, we used 1,000 pure red noise time series). However, because the Lomb-Scargle periodogram tends to overestimate the power at the high-frequency end of the spectrum, a further correction is necessary before comparing the Lomb-Scargle periodograms of the atmospheric time series against the red noise time series. This bias correction is achieved by calculating the ratios of the mean of the simulated red noise spectra against an ideal noise spectrum and using these ratios as correction factors. The issue of correctly accounting for colored noise in Lomb-Scargle periodograms is a complicated issue and a topic of active research (VanderPlas, 2018).

We use the Lomb-Scargle periodogram to search for any influence of mountains on late afternoon data, that is, a periodicity in the albedo of one solar day (116.75 Earth days). Kitahara et al. (2019) recognized a mountain-induced wave at 365 nm only once, on 17 May 2016. This implies that any UV contrast introduced by such waves is simply too small to be recognized. We also expect to see a different albedo periodicity for other local times because the mountain-induced waves are only fully developed in the late afternoon (Kouyama et al., 2017; Navarro et al., 2018; Kitahara et al., 2019). We use data in the 30–35°S latitude range to avoid data irregularities at the limb of the polar viewing images. The mountains are a little more to the north, but their influence extends to this latitude range (Kitahara et al., 2019; Kouyama et al., 2017). The resulting periodogram is shown in Figure 9 for the afternoon data. There is a periodicity peak around one solar day,

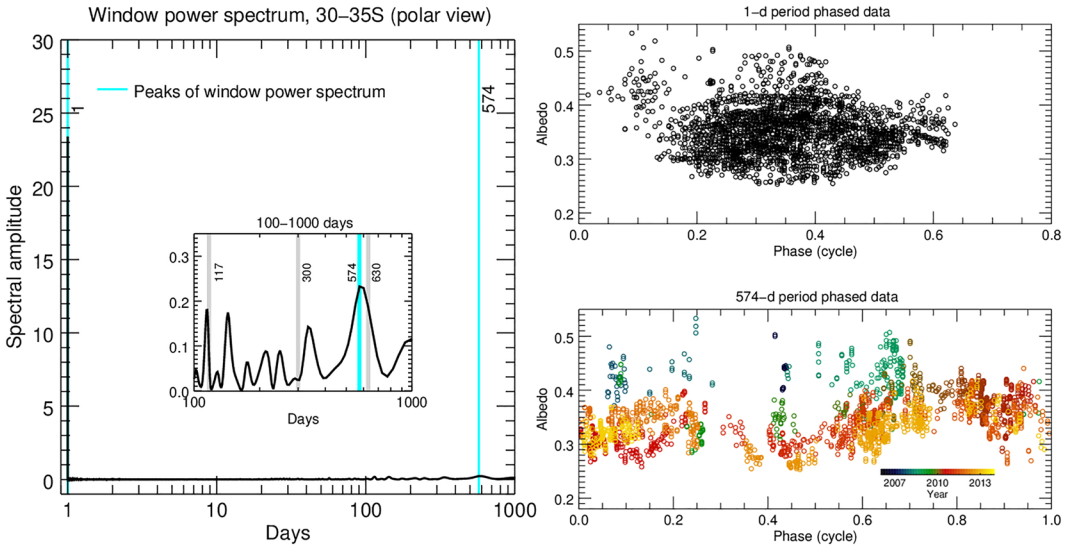

Figure 10. The window power spectrum of the data at 30–35°S latitude for polar view images. Cyan lines and their numbers indicate the detected peaks. Gray lines and their numbers are the periods described in Figure 9. A clear peak is at 1 day, and a weak peak is at 574 days shown in the enlarged plot. The right column shows albedo data as a function of phase at the detected periods: 1 day (upper right) and 574 days (bottom right). Color means years of imaging time.

but it is just at the level of the red noise (the enlarged panel) and below the 95% confidence level. There are two peaks at the 95% confidence level, located at ~300 and 630 days. These are not integer multiples of the solar day. We estimated the albedo amplitudes of these periods by fitting a sinusoidal model to the data, and they are 0.03 and 0.04, respectively (right column of Figure 9). These 300- and 630-day periods might be related to eastward-propagating centrifugal waves (Peralta et al., 2014). We checked the window power spectrum of the data (VanderPlas, 2018), as shown in Figure 10. There is an obvious data sampling period of 1 day, which is caused by the 24-hr orbital period of Venus Express and the data selection criteria (i.e., the

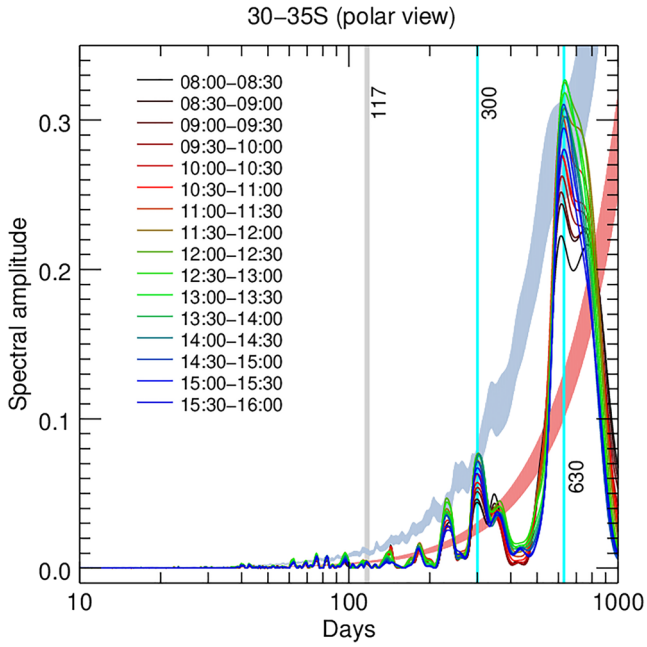

Figure 11. Lomb-Scargle periodograms at 30–35°S latitude for polar view images for all local times. The time series of 8:00–8:30, 11:30–12:00, and 15:30–16:00 hr are shown in Figure 7. The periodogram for 15:30–16:00 hr is the identical to Figure 9 (left). The red-shaded area means the red noise area over all local times, and the blue-shaded area indicates the 95% confidence limit.

90–95° phase angle bin and the polar view). There is a much weaker peak at 574 days. This peak may reflect the changes in sampling density of images over time, as sampling density increased in the second half of the observing period (bottom pannel of Figure 1). As the 574-day period is close to the 630-day period in Figure 9, the latter might be associated with the data sampling density change. Acquiring data with a longer time coverage could confirm the existence of the 630-day period.

At the cloud top level, there are strong zonal winds, which take 4–5 days to rotate the planet. This caused a 4- to 5-day period in albedo found previously (Rossow et al., 1980; Lee et al., 2015; Imai et al., 2019). However, we do not find this peak in Figure 9. This is probably due to the low density of data sampling over the 2006–2014 period due to the strict data selection criteria, which cannot capture such short-term periodic changes. For example, without the polar viewing restriction, Lee et al. (2015) detected a ~5-day peak at the same solar phase angle bin. To detect the 4- to 5-day period, one could check a subset of the data, as the strength of the 4- to 5-day period is reported to be variable over time (Del Genio & Rossow, 1990; Kouyama et al., 2013; Imai et al., 2019).

We repeated the same periodogram calculations for all local time bins, as shown in Figure 11. There are no peaks around the period of one solar day, from morning to afternoon. This may mean that mountain-induced waves have an amplitude at 365 nm below the red noise level. The peaks at 61, 75, 77, and 83 days are slightly higher than the 95% significance limit, depending on the local time bins, but their origin is not clear.

5. Summary

We found that temporal variations of the 365-nm albedo dominate over any systematic variations along longitude or over local time. We showed that the longitudinal dependence of the albedo is difficult to determine. The longitudinal coverage of dayside imaging moved slowly over the years, so the mean albedo at a specific observation time is strongly affected by temporal variations.

We investigated whether albedo depends on local time using only south pole viewing images. We noticed a subtle local minimum of albedo at low latitudes around noon, which might be related to lower abundance of SO_2 gas at noon at low latitudes (Encrenaz et al., 2019; Marcq et al., 2020). However, we cannot quantify the local time dependence of the albedo, due to a possible imperfect photometric correction.

Our periodicity analysis of the albedo in the early morning and late afternoon in the 30–35°S latitude range revealed no peak around the value of one solar day. This implies that the influence of mountain-induced waves on the UV albedo is negligible compared to other natural albedo variations.

Appendix A: Longitudinal Dependence of Mean Albedo, Corrected Using the Putative Sensor Degradation Ratio

We checked whether the albedo distributions along longitude would change if we used the sensor degradation ratio correction from Shalygina et al. (2015) (see section 2.2). We used a ratio ($k_d = -14.0 \times 10^{-5}$ [orbit^{-1}]) as applied to the PSA data (ftp://psa.esac.esa.int/pub/mirror/VENUS-EXPRESS/VMC/VEX-V-VMC-3-RDR-V3.0/DOCUMENT/VMC_INFLIGHT_CALIBRATION.TXT):

$$R_{\mathrm{obs}}(t=0) = R_{\mathrm{obs}}(t)\left(\frac{1}{1+k_d \times t}\right), \tag{A1}$$

where t is the orbit number.

The 10–15°S albedo data distributions as a function of time and longitude are shown in Figure A1 for the six phase angle bins (same as Figure 4), and the longitudinal mean albedo at 10–15°S are shown in Figure A2 (same as Figure 5). The mean longitudinal trend of Bertaux et al. (2016) (red curve in Figure A2) only resembles the trend for the data in the 75–80° and 80–85° phase angle bins before 2010. All data in other phase angle bins have different trends. So even when we use the sensor degradation ratio, the main conclusion of this study do not change: The longitudinal albedo trend in Bertaux et al. (2016) is most likely an artifact of the data sampling.

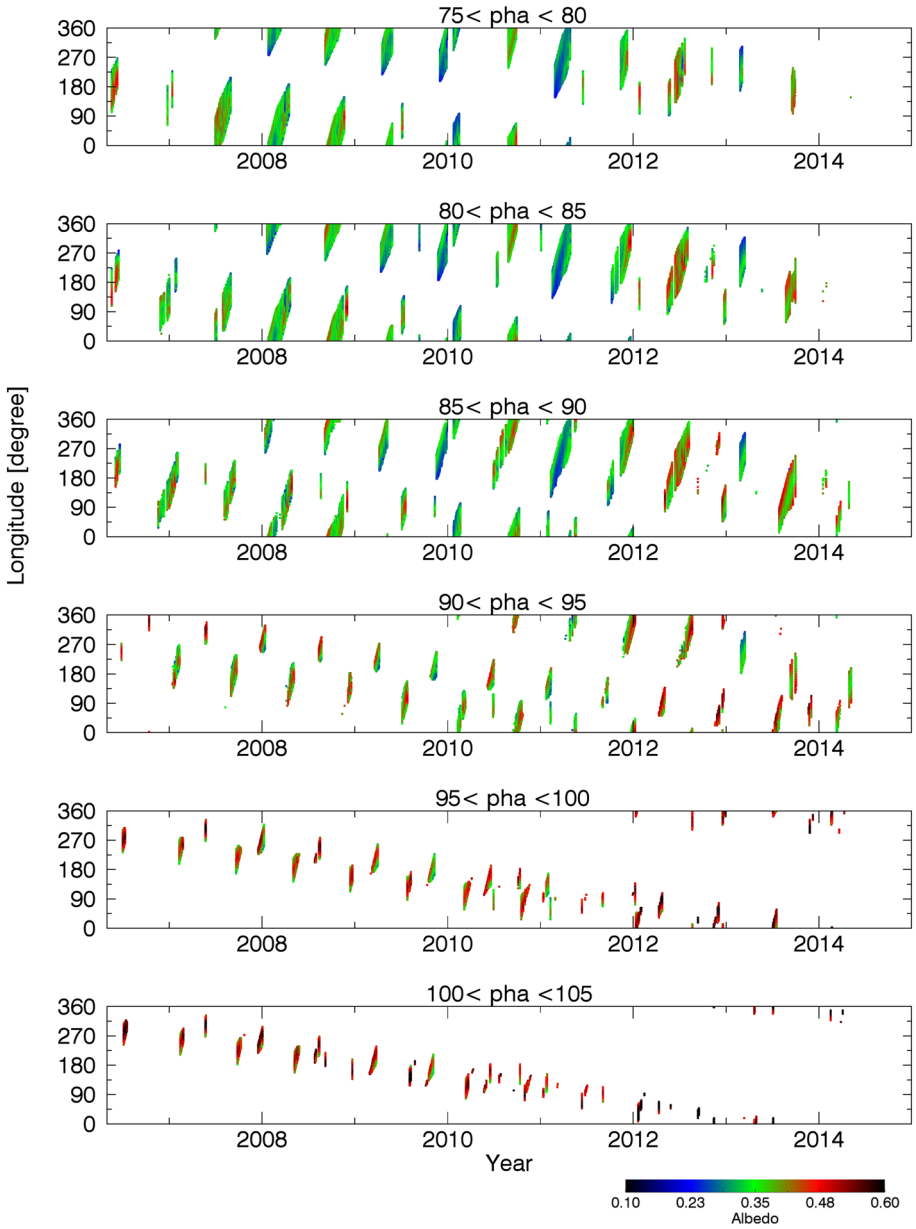

Figure A1. Same as Figure 4 but using equation (A1).

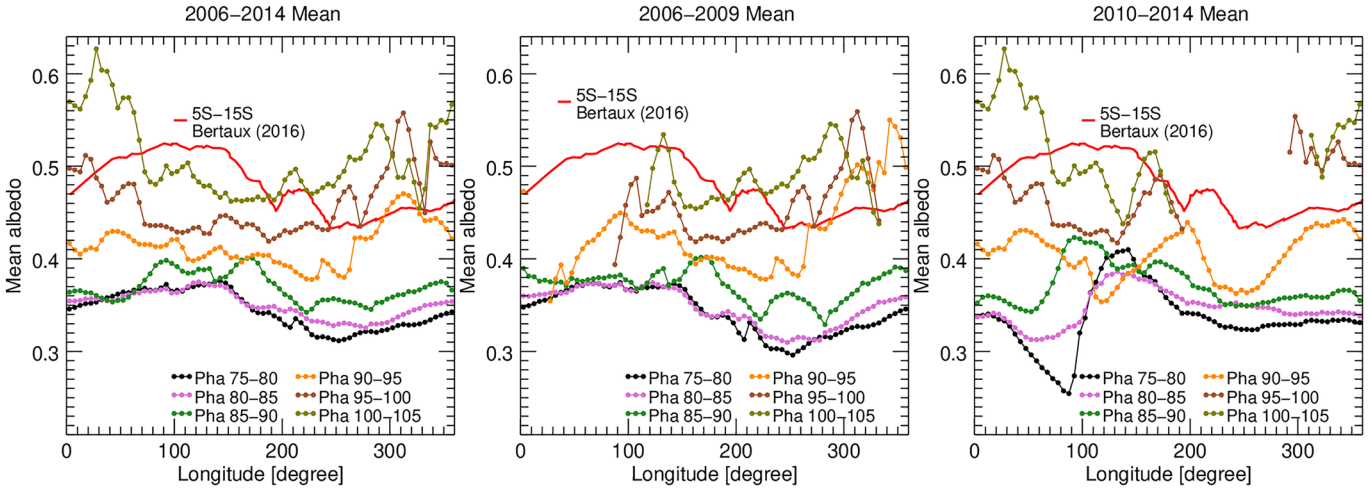

Figure A2. Same as Figure 5 but using equation (A1).

Acknowledgments

Y. J. L. has received funding from EU Horizon 2020 MSCA-IF No. 841432. P. K. was funded by the Japan Society for the Promotion of Science International Research Fellow Program. J. P. acknowledges the Japan Aerospace Exploration Agency's International Top Young Fellowship (ITYF). VMC data are publicly available at ESA PSA (ftp://psa.esac.esa.int/pub/mirror/VENUS-EXPRESS/VMC/). UVI data are publicly available at the JAXA archive website, DARTS (http://darts.isas.jaxa.jp/), and the NASA archive website, PDS (https://pds.nasa.gov/). The derived data set presented in this study and the code used for the periodicity analysis can be found online (at http://doi.org/10.5281/zenodo.3754455).

References

Bertaux, J.-L., Khatuntsev, I. V., Hauchecorne, A., Markiewicz, W. J., Marcq, E., Lebonnois, S., et al. (2016). Influence of Venus topography on the zonal wind and UV albedo at cloud top level: The role of stationary gravity waves. *Journal of Geophysical Research: Planets*, *121*, 1087–1101. https://doi.org/10.1002/2015JE004958

Buratti, B., & Veverka, J. (1983). Voyager photometry of Europa. *Icarus*, *55*, 93–110. https://doi.org/10.1016/0019-1035(83)90053-2

Carlson, R. W., Piccioni, G., & Filacchione, G. (2016). Venus Express VIRTIS-M visible-channel: Diffracted and scattered light corrections. Presented at the International Venus Conference on 4–8 April 2016, Oxford, UK.

Chance, K., & Kurucz, R. L. (2010). An improved high-resolution solar reference spectrum for Earth's atmosphere measurements in the ultraviolet, visible, and near infrared. *Journal of Quantitative Spectroscopy & Radiative Transfer*, *111*, 1289–1295. https://doi.org/10.1016/j.jqsrt.2010.01.036

Crisp, D. (1986). Radiative forcing of the Venus mesosphere. I—Solar fluxes and heating rates. *Icarus*, *67*, 484–514. https://doi.org/10.1016/0019-1035(86)90126-0

Del Genio, A. D., & Rossow, W. B. (1990). Planetary-scale waves and the cyclic nature of cloud top dynamics on Venus. *Journal of the Atmospheric Sciences*, *47*, 293–318. https://doi.org/10.1175/1520-0469(1990)047<0293:PSWATC>2.0.CO;2

Encrenaz, T., Greathouse, T. K., Marcq, E., Sagawa, H., Widemann, T., Bézard, B., et al. (2019). HDO and SO_2 thermal mapping on Venus. IV. Statistical analysis of the SO_2 plumes. *Astronomy & Astrophysics*, *623*, A70. https://doi.org/10.1051/0004-6361/201833511

Esposito, L. W. (1980). Ultraviolet contrasts and the absorbers near the Venus cloud tops. *Journal of Geophysical Research*, *85*(A13), 8151–8157. https://doi.org/10.1029/JA085iA13p08151

Fedorova, A., Marcq, E., Luginin, M., Korablev, O., Bertaux, J.-L., & Montmessin, F. (2016). Variations of water vapor and cloud top altitude in the Venus' mesosphere from SPICAV/VEx observations. *Icarus*, *275*, 143–162. https://doi.org/10.1016/j.icarus.2016.04.010

Frandsen, B. N., Wennberg, P. O., & Kjaergaard, H. G. (2016). Identification of OSSO as a near-UV absorber in the Venusian atmosphere. *Geophysical Research Letters*, *43*, 11. https://doi.org/10.1002/2016GL070916

Fukuhara, T., Futaguchi, M., Hashimoto, G. L., Horinouchi, T., Imamura, T., Iwagaimi, N., et al. (2017). Large stationary gravity wave in the atmosphere of Venus. *Nature Geoscience*, *10*(2), 85–88. https://doi.org/10.1038/ngeo2873

Gilman, D. L., Fuglister, F. J., & Mitchell, J. M. Jr. (1963). On the power spectrum of 'red noise' *Journal of Atmospheric Sciences*, *20*(2), 182–184. https://doi.org/10.1175/1520-0469(1963)020<0182:OTPSON>2.0.CO;2

Horinouchi, T., Kouyama, T., Lee, Y. J., Murakami, S.-y., Ogohara, K., Takagi, M., et al. (2018). Mean winds at the cloud top of Venus obtained from two-wavelength UV imaging by Akatsuki. *Earth, Planets, and Space*, *70*, 10. https://doi.org/10.1186/s40623-017-0775-3

Hueso, R., Peralta, J., Garate-Lopez, I., Bandos, T. V., & Sánchez-Lavega, A. (2015). Six years of Venus winds at the upper cloud level from UV, visible and near infrared observations from VIRTIS on Venus Express. *Planetary and Space Science*, *113*, 78–99. https://doi.org/10.1016/j.pss.2014.12.010

Imai, M., Kouyama, T., Takahashi, Y., Yamazaki, A., Watanabe, S., Yamada, M., et al. (2019). Planetary-scale variations in winds and UV brightness at the Venusian cloud top: Periodicity and temporal evolution. *Journal of Geophysical Research: Planets*, *124*, 2635–2659. https://doi.org/10.1029/2019JE006065

Khatuntsev, I. V., Patsaeva, M. V., Titov, D. V., Ignatiev, N. I., Turin, A. V., Limaye, S. S., et al. (2013). Cloud level winds from the Venus Express Monitoring Camera imaging. *Icarus*, *226*(1), 140–158. https://doi.org/https://doi.org/10.1016/j.icarus.2013.05.018

Kitahara, T., Imamura, T., Sato, T. M., Yamazaki, A., Lee, Y. J., Yamada, M., et al. (2019). Stationary features at the cloud top of Venus observed by ultraviolet imager onboard Akatsuki. *Journal of Geophysical Research: Planets*, *124*, 1266–1281. https://doi.org/10.1029/2018JE005842

Kopparla, P., Lee, Y. J., Imamura, T., & Yamazaki, A. (2019). Principal components of short-term variability in the ultraviolet albedo of Venus. *Astronomy & Astrophysics*, *626*, A30. https://doi.org/10.1051/0004-6361/201935388

Kouyama, T., Imamura, T., Nakamura, M., Satoh, T., & Futaana, Y. (2013). Long-term variation in the cloud-tracked zonal velocities at the cloud top of Venus deduced from Venus Express VMC images. *Journal of Geophysical Research: Planets*, *118*, 37–46. https://doi.org/10.1029/2011JE004013

Kouyama, T., Imamura, T., Taguchi, M., Fukuhara, T., Sato, T. M., Yamazaki, A., et al. (2017). Topographical and local time dependence of large stationary gravity waves observed at the cloud top of Venus. *Geophysical Research Letters*, *44*, 12,098–12,105. https://doi.org/10.1002/2017GL075792

Krasnopolsky, V. A. (2017). On the iron chloride aerosol in the clouds of Venus. *Icarus*, *286*, 134–137. https://doi.org/10.1016/j.icarus.2016.10.003

Lee, Y. J., Imamura, T., Schröder, S. E., & Marcq, E. (2015). Long-term variations of the UV contrast on Venus observed by the Venus Monitoring Camera on board Venus Express. *Icarus*, *253*, 1–15. https://doi.org/10.1016/j.icarus.2015.02.015

Lee, Y. J., Jessup, K.-L., Perez-hoyos, S., Titov, D., Lebonnois, S., Peralta, J., et al. (2019). Long-term variations of Venus' 365-nm albedo observed by Venus Express, Akatsuki, MESSENGER, and Hubble Space Telescope. *The Astronomical Journal*, *158*(3), 126. https://doi.org/10.3847/1538-3881/ab3120

Lee, Y. J., Yamazaki, A., Imamura, T., Yamada, M., Watanabe, S., Sato, T. M., et al. (2017). Scattering properties of the Venusian clouds observed by the UV imager on board Akatsuki. *Astronomical Journal*, *154*, 44. https://doi.org/10.3847/1538-3881/aa78a5

Limaye, S. S., Mogul, R., Smith, D. J., Ansari, A. H., Słowik, G. P., & Vaishampayan, P. (2018). Venus' spectral signatures and the potential for life in the clouds. *Astrobiology*, *18*, 1181–1198. https://doi.org/10.1089/ast.2017.1783

Luginin, M., Fedorova, A., Belyaev, D., Montmessin, F., Wilquet, V., Korablev, O., et al. (2016). Aerosol properties in the upper haze of Venus from SPICAV IR data. *Icarus*, *277*, 154–170. https://doi.org/10.1016/j.icarus.2016.05.008

Marcq, E., Jessup, K.-L., Baggio, L., Encrenaz, T., Lee, Y. J., Montmessin, F., et al. (2020). Climatology of SO_2 and UV absorber at Venus' cloud top from SPICAV-UV nadir dataset. *Icarus*, *335*, 113,368. https://doi.org/10.1016/j.icarus.2019.07.002

Markiewicz, W. J., Titov, D. V., Limaye, S. S., Keller, H. U., Ignatiev, N., Jaumann, R., et al. (2007). Morphology and dynamics of the upper cloud layer of Venus. *Nature*, *450*, 633–636. https://doi.org/10.1038/nature06320

McEwen, A. S. (1986). Exogenic and endogenic albedo and color patterns on Europa. *Journal of Geophysical Research*, *91*, 8077–8097. https://doi.org/10.1029/JB091iB08p08077

Mills, F. P., Esposito, L. W., & Yung, Y. L. (2007). Atmospheric composition, chemistry, and clouds. In L. Esposito, E. R. Stofan, & T. E. Cravens (Eds.), *Exploring Venus as a terrestrial planet* (Vol. 176, pp. 73–100). Washington, DC: American Geophysical Union.

Navarro, T., Schubert, G., & Lebonnois, S. (2018). Atmospheric mountain wave generation on Venus and its influence on the solid planet's rotation rate. *Nature Geoscience*, *11*(7), 487–491. https://doi.org/10.1038/s41561-018-0157-x

Peralta, J., Hueso, R., Sánchez-Lavega, A., Lee, Y. J., Muñoz, A. G., Kouyama, T., et al. (2017). Stationary waves and slowly moving features in the night upper clouds of Venus. *Nature Astronomy*, *1*, 0187. https://doi.org/10.1038/s41550-017-0187

Peralta, J., Imamura, T., Read, P. L., Luz, D., Piccialli, A., & López-Valverde, M. A. (2014). Analytical solution for waves in planets with atmospheric superrotation. II. Lamb, surface, and centrifugal waves. *Astrophysical Journal Supplement Series*, *213*(1), 18. https://doi.org/10.1088/0067-0049/213/1/18

Pérez-Hoyos, S., Sánchez-Lavega, A., García-Muñoz, A., Irwin, P. G. J., Peralta, J., Holsclaw, G., et al. (2018). Venus upper clouds and the UV absorber from MESSENGER/MASCS observations. *Journal of Geophysical Research: Planets*, *123*, 145–162. https://doi.org/10.1002/2017JE005406

Piccialli, A., Titov, D., Sanchez-Lavega, A., Peralta, J., Shalygina, O., Markiewicz, W., & Svedhem, H. (2014). High latitude gravity waves at the Venus cloud tops as observed by the Venus Monitoring Camera on board Venus Express. *Icarus*, *227*, 94–111. https://doi.org/10.1016/j.icarus.2013.09.012

Ragent, B., Esposito, L. W., Tomasko, M. G., Marov, M. I., & Shari, V. P. (1985). Particulate matter in the Venus atmosphere. *Advances in Space Research*, *5*, 85–115. https://doi.org/10.1016/0273-1177(85)90199-1

Ross, F. E. (1928). Photographs of Venus. *The Astrophysical Journal*, *68*, 57. https://doi.org/10.1086/143130

Rossow, W. B., Del Genio, A. D., Limaye, S. S., & Travis, L. D. (1980). Cloud morphology and motions from Pioneer Venus images. *Journal of Geophysical Research*, *85*, 8107–8128. https://doi.org/10.1029/JA085iA13p08107

Schulz, M., & Mudelsee, M. (2002). REDFIT: Estimating red-noise spectra directly from unevenly spaced paleoclimatic time series. *Computers and Geosciences*, *28*(3), 421–426. https://doi.org/10.1016/S0098-3004(01)00044-9

Shalygina, O. S., Petrova, E. V., Markiewicz, W. J., Ignatiev, N. I., & Shalygin, E. V. (2015). Optical properties of the Venus upper clouds from the data obtained by Venus Monitoring Camera on-board the Venus Express. *Planetary and Space Science*, *113*, 135–158. https://doi.org/10.1016/j.pss.2014.11.012

Shkuratov, Y., Kaydash, V., Korokhin, V., Velikodsky, Y., Opanasenko, N., & Videen, G. (2011). Optical measurements of the Moon as a tool to study its surface. *Planetary and Space Science*, *59*, 1326–1371. https://doi.org/10.1016/j.pss.2011.06.011

Titov, D. V., Markiewicz, W. J., Ignatiev, N. I., Song, L., Limaye, S. S., Sanchez-Lavega, A., et al. (2012). Morphology of the cloud tops as observed by the Venus Express Monitoring Camera. *Icarus*, *217*, 682–701. https://doi.org/10.1016/j.icarus.2011.06.020

Tomasko, M. G., Doose, L. R., Smith, P. H., & Odell, A. P. (1980). Measurements of the flux of sunlight in the atmosphere of Venus. *Journal of Geophysical Research*, *85*, 8167–8186. https://doi.org/10.1029/JA085iA13p08167

VanderPlas, J. T. (2018). Understanding the Lomb-Scargle periodogram. *Astrophysical Journal Supplement Series*, *236*(1), 16. https://doi.org/10.3847/1538-4365/aab766

Wright, W. H. (1927). Photographs of Venus made by infra-red and by violet light. *Publications of the Astronomical Society of the Pacific*, *39*, 220. https://doi.org/10.1086/123718

Yamazaki, A., Yamada, M., Lee, Y. J., Watanabe, S., Horinouchi, T., Murakami, S.-y., et al. (2018). Ultraviolet imager on Venus orbiter Akatsuki and its initial results. *Earth, Planets and Space*, *70*(1), 23. https://doi.org/10.1186/s40623-017-0772-6